Nanoscale Chemical Imaging of *Bacillus subtilis* Spores by Combining Tip-Enhanced Raman Scattering and Advanced Statistical Tools

Giulia Rusciano,*,† Gianluigi Zito,† Rachele Isticato,‡ Teja Sirec,‡ Ezio Ricca,‡ Elena Bailo,§ and Antonio Sasso†

†Department of Physics and ‡Department of Biology, University of Naples Federico II, via Cintia, 80126-I Naples, Italy and §WITec GmbH, Lise-Meitner-Strasse 6, DE-89081 Ulm, Germany

ABSTRACT Tip-enhanced Raman Scattering (TERS) has recently emerged as a powerful spectroscopic technique capable of providing subdiffraction morphological and chemical information on samples. In this work, we apply TERS spectroscopy for surface analysis of the *Bacillus subtilis* spore, a very attractive biosystem for a wide range of applications regulated by the spore surface properties. The observed spectra reflect the complex and heterogeneous environment explored by the plasmonic tip, therefore exhibiting significant point-to-point variations at the nanoscale. Herein, we demonstrate that TERS data processing via principal component analysis allows handling such spectral changes, thus enabling an unbiased correlative imaging based on TERS. Our experimental outcomes suggest a denser arrangement of both proteins and carbohydrates on specific spore surface regions simultaneously revealed by AFM phase imaging. Successful TERS analysis of spores' surface is useful for bacterial surface-display systems and drug delivery applications.

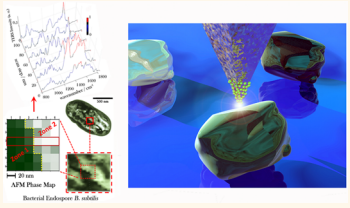

KEYWORDS: tip-enhanced Raman scattering · *Bacillus subtilis* · chemical imaging · principal component analysis (PCA)

Bacterial spores are quite fascinating biological systems. In their dormant state, which can persist even thousands of years, they are extremely resistant to environmental stress factors including heat, radiation, and desiccation.[1,2] Spore capability of enduring to extremely harsh conditions derives from its complex architecture, in which an external multishell-type structure (the coat) surrounds a central dry core containing the bacteria genome,[3−6] as schematically depicted in Figure 1a. These features have inspired a large variety of technological applications. Recently, the strong water responsivity of spores has been used to build an energy-harvesting device able to generate electrical power from an evaporating body of water.[7] More mature spores' applications regard instead spore *surface display* technology[3] for the production of biocatalists, biosensors,[3,8−12] and vaccine development.[10] Clearly, an understanding of spore coat organization is a crucial issue for a successful development of these spore-based applications. A deeper understanding of the coat architecture is also mandatory for developing coat-disassembling strategies of pathogenic spores like *Bacillus anthracis*, also used as a bioterrorism weapon.[13,14] In literature, many papers can be found regarding spore surface characterization, mainly performed by atomic force microscopy (AFM) and transmission electron microscopy (TEM).[15] Chemical analysis of the spore coat has been instead performed by Western blot analysis of solubilized extracts from the spore coat, a technique which obviously implies a complete loss of information about the chemicals' distribution on the spore surface. Although it could represent a particularly challenging issue, having a spatially resolved information which correlates the morphological spore surface features with their related chemical fingerprints can provide a deeper insight into spore coat architecture. Tip-enhanced Raman scattering (TERS) is expected to provide such information by combining the advantages of surface-enhanced Raman scattering (SERS) with those of a scanning probe microscopy like AFM. In TERS, a metallic (or metaled) tip is illuminated by a tightly focused laser beam. The metal tip acts as a highly localized nanoantenna able

* Address correspondence to giulia.rusciano@unina.it.

Received for review August 16, 2014 and accepted November 21, 2014.

Published online November 21, 2014
10.1021/nn504595k

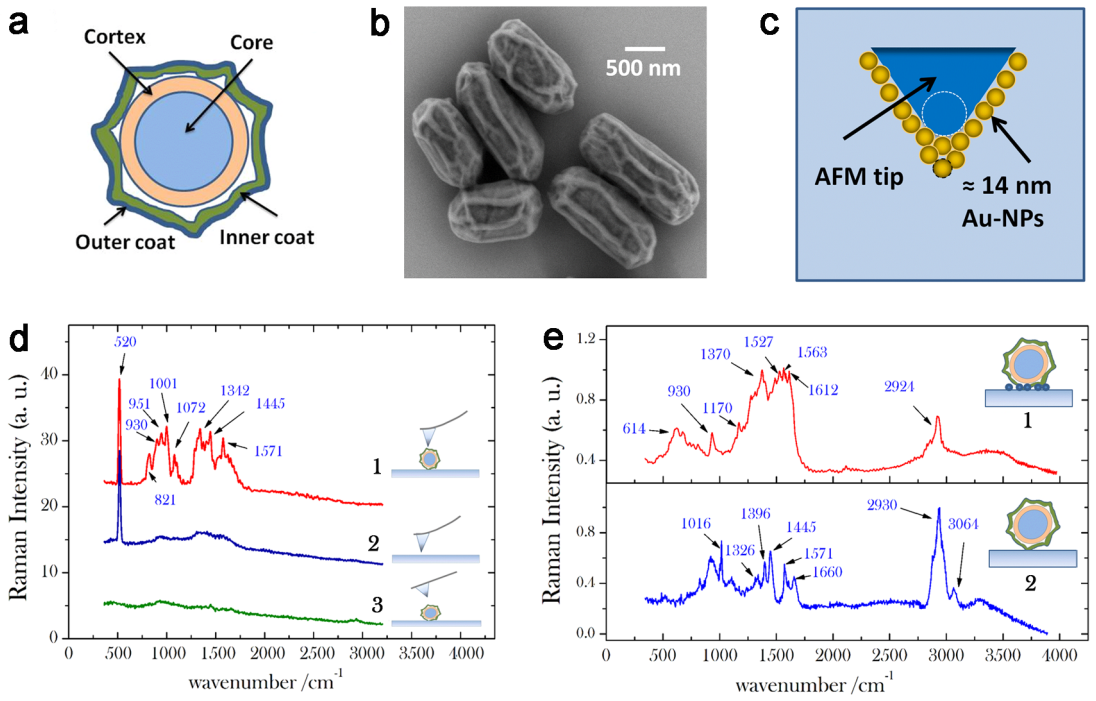

Figure 1. (a) Cartoon of the wild-type *B. subtilis* architecture: the central region defines the spore core containing calcium dipicolinate (CaDPA),[3] which houses the genomic material and protects it from the environment (see the Supporting Information). The core is surrounded by three main regions: an inner membrane, an outer cortex mainly composed of peptidoglycans, and finally an outermost multishell structure called coat. (b) SEM image of fully dehydrated *B. subtilis* spores (scale bar: 500 nm): spore surface exhibits characteristic ridges resulting from volume contraction due to the core dehydration. (c) Sketch of the TERS tip used in this work: it is a commercial AFM tip on which 14 nm Au-NPs are deposited upon ultrahigh vacuum conditions. (d) (1) Representative TERS signal from wild-type *B. subtilis* spore on tip-engaged status (incident power $P = 50\ \mu W$, integration time $\tau = 2$ s); (2) control TERS signal acquired in a clean part of the glass coverslip ($P = 50\ \mu W$, $\tau = 2$ s); (3) spectrum of the spore acquired after tip retraction in the same position of trace (1). (e) (1) A typical SERS signal of the *B. subtilis* spore acquired using Ag colloids as SERS substrate ($P = 50\ \mu W$, $\tau = 4$ s); (2) conventional confocal Raman spectrum of a *B. subtilis* spore ($P = 500\ \mu W$, $\tau = 30$ s).

to provide a strong amplification of the Raman signal via localized plasmon resonances excited at the tip apex.[16,17] Therefore, this technique combines the chemical fingerprint recognition provided by Raman spectroscopy with a nanoscale near-field resolution. The simultaneous recording of both topographical and chemical information provided by TERS technique has, in very recent years, allowed a deeper insight into the surface properties of many systems at the nanoscale,[18,19] including biosystems.[20−26] In particular, TERS analysis has been focused on the investigation of DNA- and RNA-based systems,[27−34] as well as protein-related systems.[17,35−37] Recently, notable progress has also been achieved for more *complex* biosystems such as single amyloid fibril,[38] alginates,[39] insulin protofilaments,[40] virus,[41] and hemozoin crystals[42] as well as synthetic[43] or real cellular membranes.[44−48]

Herein, we demonstrate that TERS technique is capable shedding light on spore coat organization when processing the surface maps through advanced statistical tools. In particular, this work concerns TERS investigation of spores from wild-type *Bacillus subtilis* bacteria, which are often considered as a model system for spore-forming bacteria.[3] The complexity and heterogeneity of bacterial spore surface structure requires a careful analysis of the spectral features revealed in TERS spectroscopy. Remarkably, despite the fact that TERS surface scans are characterized by spectral features spatially varying on the nanoscale and difficult to interpret, we are able to discriminate the relevant characteristics of spore surface chemistry by taking advantage of basis analysis (BA)[49] and principal components analysis (PCA),[50,51] which allow us to generate statistically significant TERS-based chemical maps. The PCA maps result in strong correlation with the nanoscopic-resolved observation provided by the simultaneous AFM phase mapping, independently providing a spatial distribution of the surface composition, adhesion, friction, and viscoelastic properties of the cell, hence, a signature of a chemical differentiation. From *a posteriori* reconstruction of the statistically relevant Raman spectra, we speculate about the molecular spatial distribution along the so-called spore ridges, readily distinguishable in the scanning electron micrograph shown in Figure 1b along the spore long-axis. The ridge's function is probably connected to the spore capability to accommodate volume changes occurring during spore core dehydration and rehydration.[52] Our results point out a denser arrangement of proteins with an increased outer concentration of carbohydrates along the ridge.

RESULTS AND DISCUSSION

The TERS setup we used is based on the WITec Alpha 300 system and consisted of an AFM system mounted on an inverted Raman microscope (see the Supporting Information, Figure S1). For excitation, a linearly polarized laser at 532 nm was focused on the sample through a 60× dry objective (NA = 0.8). Under this operative condition, a beam waist of 370 nm was accurately measured at the laser focus. For TERS analysis, 50 μL of a water suspension of mature PY79 wild-type spores at a concentration of 10^5 spore/mL were pipetted on a clean microscope glass coverslip and left to dry at ambient conditions. The coverslip was mounted on a 3D piezo-scanner (P-500, Physik Instrumente) above the optical microscope. TERS tips were provided by Next-Tip S. L. (Madrid, Spain). They consisted of commercial AFM tips with elastic constant of ~2.8 N/m and resonance frequency at ca. 75 kHz on which controlled-size gold nanoparticles (Au-NPs) were deposited upon ultrahigh vacuum conditions. A schematical representation is given in Figure 1c. As demonstrated in previous works, the deposition of nanometric Au-NPs increases the resolution in both topography[53] and Kelvin probe force microscopy or surface potential microscopy.[54,55] In our case, larger Au nanoparticles with a diameter ~14 nm were deposited on Si-based tips as a compromise between large-enough surface-enhanced Raman signal and reasonably accurate spatial resolution. Such a procedure gave rise to high-performance, reliable, and stable TERS tips.

Before TERS investigation, AFM mapping was performed to ensure tip engagement with laser off. In particular, in order to prevent tip-induced artifacts caused by the interaction of the tip with the relatively soft spore surface, AFM analysis was performed in tapping mode. Then, tip engagement was iteratively corrected with laser on. Subsequently, the tip was moved to the desired position and optimum spectroscopic signal enhancement was searched, while the tip was retained under approaching conditions, by finely matching the laser focus with the tip apex by means of a piezo-driver controlling the focusing objective. This procedure was facilitated by the observation of the Raman signal from the bulk Si of the tip. Once signal optimization was achieved, the TERS signal was collected. For comparison, a Raman signal was collected under tip-retracted conditions as well.

The results of this procedure are reported in Figure 1d. In particular, trace 1 corresponds to the TERS spectrum $I_{tip\text{-}in}$ acquired with the tip in contact with the sample; trace 2 corresponds to the signal I_{tip} acquired with the tip placed on a *clean* part of the glass coverslip; finally trace 3 reports the background far-field signal $I_{tip\text{-}out}$ acquired under tip retracted conditions (retaining the other experimental conditions). Interestingly, the latter signal exhibited no significant Raman peaks, as a consequence of the low Raman activity of the spore and the relatively low excitation power and integration time, respectively P = 50 μW and τ = 2 s. On the contrary, under the enhancement conditions provided by the tip, the TERS spectrum revealed many bands in the region between 600 and 1600 cm^{-1} (trace 1), along with the silicon-bulk-tip peak at 520 cm^{-1}. These bands mainly arise from the external coat of the spore, with minimal contribution from amorphous carbon adsorbed on the tip surface as confirmed by acquiring the signal I_{tip} (Figure 1d, trace 2). It is also worth noticing that TERS spectra were remarkably different from the confocal Raman spectrum of the spore reported in trace 2 of Figure 1e: in this case, the spectrum reflects the average bulk Raman response mainly dominated by the calcium dipicolinate contained in the inner spore core. Instead, TERS spectrum presents several enhanced features also present in the *B. subtilis* spore SERS spectrum that was measured in an independent experiment with a silver colloidal substrate[56] (trace 1 of Figure 1e). Clearly, the common enhanced features reflect the same surface origin of both SERS and TERS signals. On the other hand, the difference that can be seen between the SERS and TERS spectra mainly reflects the difference between the far-field information provided by SERS (integral laser scattering area) against the near-field information provided by TERS (local scattering at the tip position). It should be also pointed out that, once the tip approach was completed, the TERS signal was quite stable (within the noise) even for tens of seconds. In particular, we did not observe the TERS signals fluctuactions reported in other investigations (*e.g.*, refs 28,43, and 46). As reported by Neugebauer *et al.*,[46] excluding the eventual contribution to tip oxidation/contamination, TERS signals fluctuactions in biosystems are mainly due to the dynamic of molecules near the tip-apex so that their presence/absence strongly depends on the fluidity of the investigated biosurface,[43] as well as by the environment in which it lies. Therefore, the absence of fluctuations of TERS signal could be likely ascribed, in our case, by the fact that bacterial spores do not have an external soft membrane (as a vegetative cells) but rather an electron-dense outer layer (the coat). In such a structure, a quite reduced mobility can be expected from the layer molecules. It also should be noticed that our measurements were performed on dry sample, and this probably contributed to the reduction of the diffusion capability of molecules near the tip region. Signal stability was an important prerequisite to get reliable and quantitative experimental outcomes.

By comparing the near-field interaction spectrum I_{NF} and the far-field background signal intensity I_{FF} at a given spectral position, it is possible to estimate the so-called optical contrast OC through the relation:[39]

$$OC = \frac{I_{NF}}{I_{FF}} = \frac{I_{tip\text{-}in} - I_{tip\text{-}out} - I_{tip}}{I_{tip\text{-}out}} \quad (1)$$

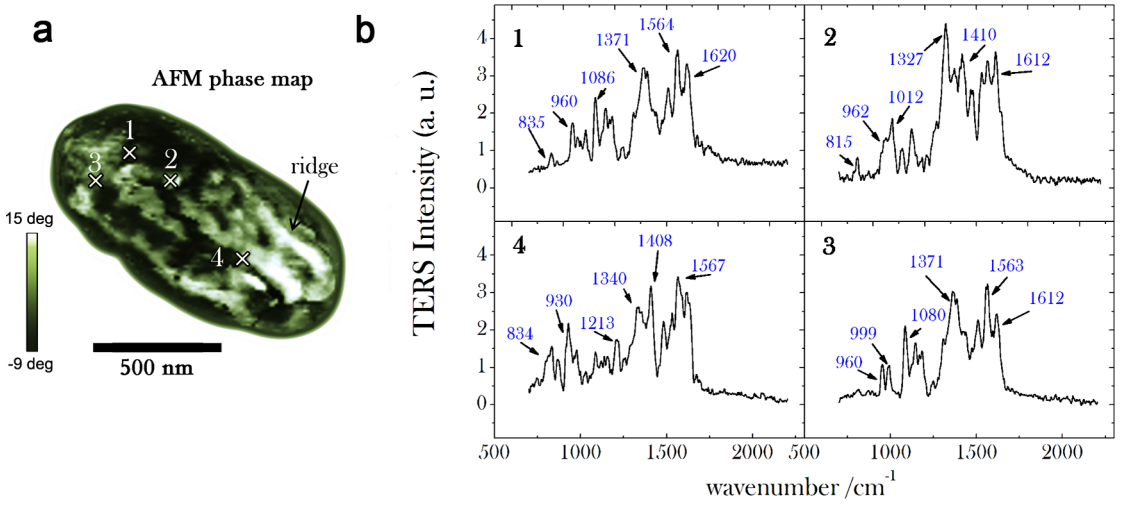

Figure 2. (a) AFM phase map of a whole spore acquired in tapping mode (scale bar = 500 nm, step-size = 20 nm): bright (dark) zones correspond to a positive (negative) phase-lag, namely to regions of higher (lower) stiffness. (b) Near-field (normalized) TERS spectra acquired in four selected positions over the spore coat, corresponding to the cross-marks in (a): in order to emphasize the relevant Raman features, background signal is identified by a fourth-order polynomial fitting routine and consequently subtracted.

By evaluating the intensity of the peak at 1001 cm^{-1}, we obtained a value OC = 55. From this, we estimated the field enhancement factor g through the relation[57]

$$OC = \frac{A_{NF}}{A_{FF}} g^4 \qquad (2)$$

where A_{NF} and A_{FF} represent, respectively, the tip-enhanced and confocal scattering area. In a conservative approach, we have assumed $A_{NF} = \pi r^2 \sim 310\ nm^2$, where r defines an effective radius of the metaled tip estimated, as discussed below, by considering the spatial resolution evidenced by TERS mapping and the geometry of the tip apex. The scattering area was instead measured by knife-edge scanning of the laser beam at the focus plane, which gave $A_{FF} = 4.3 \times 10^5\ nm^2$. Therefore, we derive $g \sim 17$, which is in reasonable agreement with other values reported in literature.[34,57,58]

In order to test the surface chemical heterogeneity, we acquired TERS spectra by positioning the tip in several points of the spore surface. Figure 2a shows the preliminary (laser off) AFM phase-map of the particular spore analyzed. While ridges along the surface of the spore were clearly evidenced in the phase-map, the corresponding topography did not show any relevant morphological features since the spore was probably still partially hydrated.[52] Interestingly, near-field TERS probing exhibited a marked point-to-point variation but also common spectral features in many spectra. As can be seen from Figure 2b, characteristic Raman bands were found to lie in the range between 500 and 1600 cm^{-1}, and these can be attributed to well-known vibrational groups, as reported in Table 1. Instead, features in the spectral range between 1640 and 1690 cm^{-1} were only occasionally visible in the TERS spectra. This circumstance seems to confirm the general finding reported in many previous TERS investigations.[59−61] However, the absence of sharp peaks in this region could be also ascribed to the simultaneous presence of many proteins within the enhancing tip region, likely giving rise to broad spectral features rather than sharp peaks.

TABLE 1. Tentative Assignment of the Main TERS Bands Observed in This Work

obsd shift (cm^{-1})	assignment	ref
830	ν_{as}(O−P−O), ν_{ring}(C−C) (Tyr)	44, 38, 46
930	δ(C−C−O)	39
1001	ν(C−C) (aromatic ring) (Phe)	46, 44
1030	ν(C−C)	46, 44
1091	$\nu_s(PO_2)$, glycosidic ring breathing	46, 44, 39, 48
1128	glycosidic ring breathing	39
1205	ν(CO−O−C), $\nu_{as}(PO_2)$, amide III (Tyr, Phe)	46 44 48,
1338	amide II (Trp)	46
1373	$\nu_s(COO^-)$, $\delta(CH_3)$	39 44,
1445	$\delta(CH_2)$, $\delta(CH_3)$	44
1546	amide II	44
1574	amide II (Phe, Trp)	38

As reported in ref 6, biochemical assays performed on spore extracts have pointed out a coat protein composition particularly rich in tyrosine and cysteine amino acids, whereas carbohydrates and lipids were present only in a small relative concentration of 5% w/w, apparently in contrast with the frequent occurrence of carbohydrate-related spectroscopic signatures in our TERS spectra. Our finding can be explained by speculating that the glycosides groups in both glycoproteins and carbohydrates are concentrated in the outermost coat shell, termed *crust*,[3] thereby experiencing a relatively high enhancement upon tip contact. Such interpretation is indeed consistent with the electron microscopy results reported by Waller *at al.* found

on ruthenium red stained *B. subtilis*, which evidenced the presence of an external glycoprotein layer surrounding the spore.[62]

An important issue addressed in the present work relies on the generation of TERS-based images correlated with AFM maps. For particular samples like carbon nanotubes which exhibit very well-identifiable spectral markers, this analysis can be straightforward, and an example is discussed in the Supporting Information (Figure S2). On the other hand, when dealing with complex systems (such as biosystems), the generation of TERS maps reporting the spatial distribution of Raman intensity integrated over an assigned band may give rise to false interpretations, since often the presence/absence of only one spectral feature is not informative. A complex molecular diversity, on the nanoscale, may hamper dramatically the identification of a significant spectral label for constructing *really informative* TERS maps. Even more difficult is correlating TERS imaging with other nanoscopic observations, like the viscoelastic properties reflected in the AFM phase maps. Recently, Richter *et al.* reported on a TERS investigation of human colon cancer cells (HT29).[48] The TERS spectra, acquired on a 162 nm × 270 nm area, were analyzed by using a statistical approach based on an algorithm (N-FINDR) which decomposes each acquired spectrum as a superposition of *endmembers*, selected as the most dissimilar spectra spanning the largest volume in the spectral space. With this approach, the authors highlighted the presence of protein and lipid domains in the cell membrane. No correlation with AFM maps was searched for though. Later, the paper by Pozzi *et al.*[20] suggested the necessity of adopting advanced data analysis tools like principal component analysis to unravel the information provided by TERS spectra acquired during surface scans. With this in mind, we decided to analyze TERS maps making use of statistical tools such as basis analysis and principal component analysis.

TERS maps were acquired by using a low laser power (~50 μW) in order to avoid sample photodamage. The occurrence of sample photodamage was checked by monitoring the Raman signal stability under prolonged (~30 min) laser exposure. To compensate the intrinsic low Raman activity of this biological sample,[63] we used an integration time of ca. 2 s. We found the *thick* (~600 nm) structure of the spore to dramatically affect the optimal matching required for TERS between the laser beam focus and the tip. In more detail, once finely tuned the TERS signal at one fixed position, displacing the tip at distances above a hundred of nanometers from that position, led to the complete loss of the backscattered TERS signal, eventually disabling any successful TERS mapping when scanning areas larger than 150 nm (of side) over the spore surface. Therefore, we limited TERS mapping to sampling windows with side of ~120 nm. This was also necessary for controlling the simultaneous acquisitions of AFM phase maps and TERS data in a reproducible fashion. Numerous TERS maps were acquired in different regions. Then we focused our attention on the ridges evidenced in AFM-phase map of *B. subtilis* spore bacteria.

Spore ridges, mainly extended along the spore long axis (Figure 1b), are commonly observed in AFM-height maps of fully dehydrated spores and are thought to be associated with the spore volume contracting upon core dehydration,[64] which is also consistent with their almost complete disappearance under high environmental humidity.[52] In our case, only minimal ridge-like structures were observed in AFM-height maps, which is consistent with an incipient core dehydration. Instead, highly contrasted ridges were observed in the AFM-phase map (Figure 2a). These features correspond to surface regions exhibiting different interactions with the near-field probe. Micro- and nanotextured AFM-phase maps have been reported in literature for several spore strains.[65,66] These maps are generally considered more useful than the simple surface topography to discriminate among different spore strains.[66] To the best of our knowledge, no information is actually reported on the surface distribution of chemicals on the coat related to the spore ridges. In order to provide insight on the surface ridge observed in our investigation, TERS maps were acquired across the ridge borders, *i.e.*, approximately around the boundaries defined by the zero-phase crossing lines in the phase map.

By mapping the phase of the oscillating cantilever in tapping mode, AFM phase imaging detects spatial variations in material composition and properties like adhesion, friction and viscoelasticity, thereby differentiating regions of high and low surface adhesion or hardness. We started from the hypothesis that a chemical diversity existed between ridges and other spore regions consistently with the different viscoelasticity (or composition) detected in the phase map (Figure 2a). Therefore, we applied TERS imaging protocols based on selected peak intensity maps, zone-average basis spectra, and principal component analysis to highlight this difference. Figure 3a shows the TERS spectra acquired along a row of a 120 nm × 120 nm raster scan performed with step of 20 nm. The corresponding row in the phase map is highlighted in red in Figure 3b. In addition, the TERS spectra corresponding to all points of the raster scan are also provided in the Supporting Information (Figure S3). Interestingly, TERS spectra of Figure 3a, although acquired in consecutive positions, exhibited a marked point-to-point variation. The colormap emphasizes some details. These reproducible spectral variation indicated a lateral resolution in the scanned surface-chemistry, comparable with the scale of the scan step (20 nm).[20] We used one-half pixel size of the scan as effective radius of the near-field probe apex

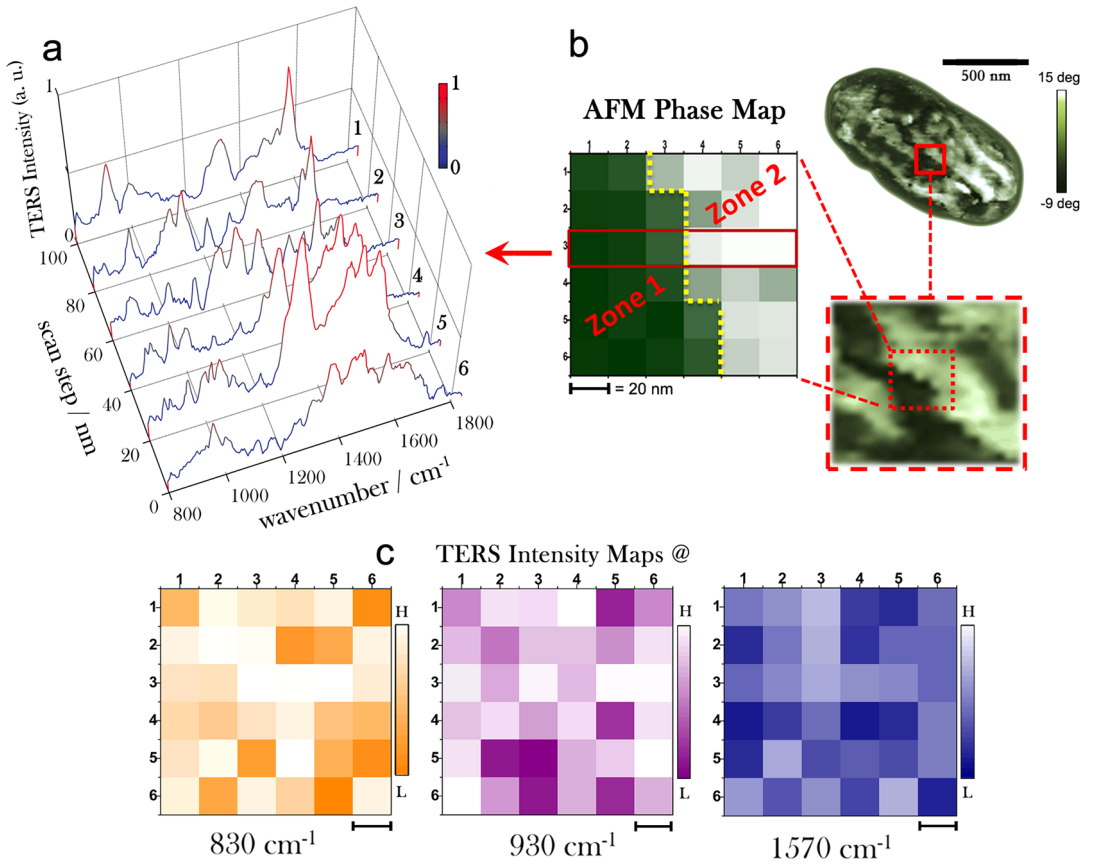

Figure 3. (a) Waterfall representation of TERS spectra acquired with 20 nm step along the horizontal line highlighted by the red rectangle in the phase map zoom of panel (b) ($P = 50\ \mu W$, $\tau = 2$ s). (b) AFM phase map and detailed zoom of a selected spore region across a spore ridge: the dashed line defines the border between two zones around the zero-crossing. In particular, zone 2 (exhibiting an higher stiffness) corresponds to a surface ridge. (c) TERS maps were obtained by projecting the intensity of Raman peaks at 812, 930, and 1570 cm^{-1}, as indicated in the labels. Scale bar = 20 nm. Color bar: L = low level, H = high level.

to estimate the OC quantity previously introduced in eq 2.

The TERS spectra acquired along the surface raster scan of Figure 3b were first processed by evaluating the strengths of selected Raman bands, as shown in Figure 3c. Figure 3c reports the maps corresponding to Tyrosine peak at 830 cm^{-1}, the peak at 930 cm^{-1} due to glycans/carbohydrates, and the aspecific feature around 1570 cm^{-1} (mainly due to proteins) prominent in several TERS spectra (Figure S3, Supporting Information). The colormap is built by scaling to one the maximum (white) level. None of them suggests any direct correspondence to the phase map, meaning that the selected peaks are not able to provide the required information about the chemical spatial diversity expected for the two zones of Figure 3b. Similar results have been obtained for all observed spectral features. The large variability of the TERS spectra due to the heterogeneity of the environment explored by the tip made the application of BA difficult as well, since the choice of the basis functions was not trivial. However, an attempt was made by imposing as basis functions the average spectra of the two zones appearing in the phase map across the ridge and indicated as zones 1 and 2 (Figure 4b). Such average TERS spectra are shown in Figure 4a. The corresponding BC maps are shown on the right part of same panel (Figure 4a). By this choice, we were able to recognize a spatial distribution in the BC maps to some extent correlated with the phase-map zones, again reported in Figure 4b just to facilitate the comparison between images. In particular, the basis component map BC2, obtained by projecting the weight of the zone-2 average spectrum (the ridge) along the scan grid, seems to be roughly confined in zone 2, whereas the BC1 map, corresponding to the zone-1 average, appears to be spread also in zone 2. Therefore, the results in part confirm the effective average chemical diversity of the two zones. However, it is worth noting that the basis analysis allowed us to reproduce to some extent the spatial distribution of the phase map only thanks to our biased *a priori* knowledge of the regions to differentiate as evidenced by the independent AFM signal.

Therefore, we carried out a PCA analysis on the same TERS data. With respect to BA (or other algorithm-based analyses like the N-FINDER[48]), the PCA approach presents advantages and disadvantages. For sure, BA constitutes a more direct and intuitive approach, being

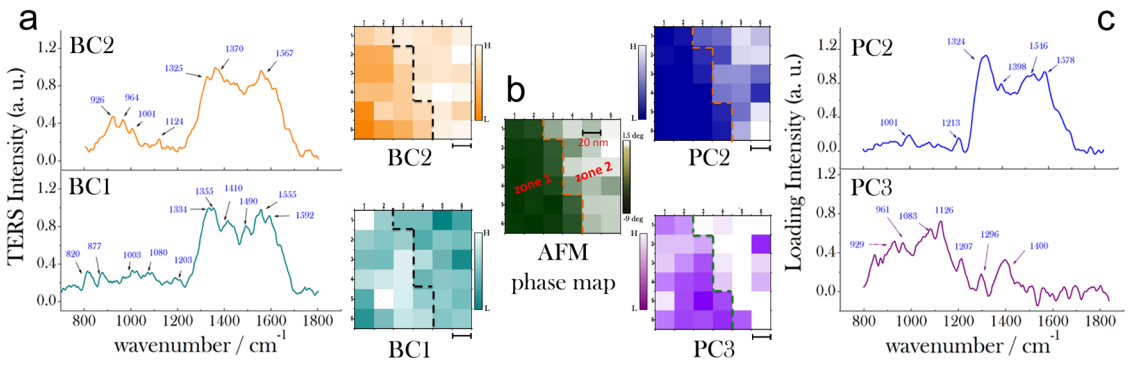

Figure 4. (a) Average TERS spectra of zone 1 and 2 (from panel (b)) defined as basis functions for basis analysis: spectra are labeled as the corresponding component maps BC1 and BC2, respectively, shown on the right part of same panel (a). (b) Detail of the AFM phase map over the same window of 120 nm × 120 nm actually measured along TERS mapping across a spore ridge. The dashed line highlights the boundary between two zones in the phase map of different stiffness: the ridge corresponds to zone 2. Scale is everywhere 20 nm. (c) PC2 and PC3 score maps (related loadings on the right) resulting from PCA analysis of same TERS data map acquired in the square region under consideration: PC-maps reveal a stronger spatial correlation with the phase map in (b). Color bar: L = low level, H = high level.

the basis functions real spectra (or average of spectra) with known spectral features. On the other hand, the successful application of this approach is conditioned by the choice of *good* basis functions, ideally the spectra of the pure chemicals present in the sample. This is obviously not straightforward in complex biological environments and surely requires the acquisition of a relevant number of spectra to properly represent all surface chemical components. By using PCA, instead, each spectrum is decomposed in principal components (PCs), obtained by analyzing the correlation of the spectral observables (*i.e.*, intensity values at given wavenumbers) (Methods). Each PC takes into account the correlated variation of the observables from spectrum to spectrum (*i.e.*, from point to point in Raman imaging). The *weight* of each variable in a given PC is described by the respective PC *loading*.[50] This latter is not a *real* spectrum (it can even present negative features in the case of anticorrelated variables) but provides information on the origin of the point-to-point variation deconvoluted by the correlation analysis. Therefore, the analysis of PC loadings is, in general, not trivial. On the other hand, PCA-based spectral analysis does not require (in principle) the acquisition of *representative* spectra. The contribution of given chemicals (proteins, lipids, or carbohydrates) is indeed provided by the correlation analysis. Therefore, with respect to algorithms based on the direct deconvolution of spectra, the PCA-based approach requires the acquisition of a lower number of spectra. The result of our analysis is shown in Figure 4c. The first three PCs were found to account for more than 80% of the total data variance. Significant maps were obtained by retaining only these components. The first loading spectrum revealed only the background contribution, giving rise to a PC1 map near uniformly spread over the whole analyzed region. Second and third PC maps of TERS data (PC2 and PC3, respectively) are reported in Figure 4c, with corresponding loadings on the right.

TABLE 2. Pearson Correlation Coefficient between the AFM-Phase Map Shown in Figure 3b and the Spectroscopic (Figure 3c) TERS Maps, as Well as the Maps Obtained by Statistical analysis of TERS Data (Figure 4b)

Pearson coefficients						
intensity maps			BA maps		PCA maps	
I_{830}	I_{930}	I_{1570}	BC1 map	BC2 map	PC2 map	PC3 map
0.11	−0.04	−0.05	−0.29	0.45	0.78	0.69

The colormap is everywhere built by scaling to one the maximum (white) level. Both PC2 and PC3 score maps nicely resemble the AFM-phase map with higher score corresponding to the ridge zone. A quantitative evaluation of map similarity has been performed by calculating the Pearson correlation coefficient P[67] between the two matrices associated with the images (Supporting Information). This coefficient is equal to 1 for fully correlated images, −1 for anticorrelated images, and 0 for not correlated images. In Table 2, we report the calculated Pearson coefficients between the AFM phase map and the PC score maps; for comparison, the Pearson coefficient was also evaluated for the BC1(2) maps as well for peak-intensity based maps of Figure 3. As it is possible to see, while a quite low P value (around zero) can be found for the peak-intensity based maps, P values definitely increase for the maps deriving from the BA and PCA analyses, reaching 0.78 for PC2-map.

An understanding of the biochemical basis of differentiation between the considered zones 1 and 2, as highlighted by PCA, can be found by inspecting the spectral features in PC2 and PC3 loadings (Figure 4c). The PC2 loading consists of relatively wide features that are systematically found on the ridge zone (see detailed spectra in Figure S3, Supporting Information). The continuity of the scanning process rules out the

possibility of a carbonaceous contamination of the tip; thus, these broad spectral features present in PC2 are more likely ascribable to a denser arrangement of protein amino acids across the ridge, as also evidenced by the intense load on phenyl ring vibration around 1570 cm^{-1}, hydrogen bonded β-turn at 1324 cm^{-1}, and phenylalanine at 1001 cm^{-1} (Figure 4c, PC2). Analogously to PC2, also the PC3 map (Figure 4c) presents important overlapping with the phase map zone 2 (Figure 4b). The sharp spectral features of the third loading (PC3) put into evidence variations in the spectral regions concerning the Raman bands of simple carbohydrates, in particular in the 900−1100 cm^{-1} region, as well as amino acids related features (Table 1). However, PC3 also exhibits some unspecific features around 1400 cm^{-1} common to proteins, lipids, and carbohydrates. We speculate that PC3 score map could represent a higher concentration of simple sugars on the ridge surface, responsible of the higher stiffness evidenced in the phase map. In this frame, the ridge might act as a sort of chemical reservoir for bacteria after sporulation of the dormant cell. The analysis was repeated in other regions across the ridge obtaining similar results as reported in the Supporting Information, Figure S4. On the other hand, in a phase-homogeneous region (*i.e.*, not across a ridge), the analysis of the related TERS signals was characterized by score maps with no clustered-scores areas (Supporting Information, Figure S5), probably because of the more uniform distribution of the surface chemicals.

CONCLUSIONS

In summary, we report the first experimental application of tip-enhanced Raman spectroscopy on the *Bacillus subtilis* bacterial spore. We demonstrate that by taking advantage of advanced statistical tools like principal component analysis, TERS-based imaging maps can be correlated with AFM-phase maps, thus allowing one to discriminate the relevant chemical distribution of this complex biological system, otherwise nonintuitively identifiable. In particular, PCA provides very informative, *unbiased* TERS maps not dependent on the particular researcher's choice of the Raman peak intensity (or basis spectrum) represented in the map. This might be very useful for drawing solid conclusions from TERS analysis of complex organisms like spores or other cells. Supplying a robust methodology to the TERS community may also support the diffusion of this technique in many fields of science, including biology and biomedicine. In particular, our TERS imaging analysis provides information about the chemicals' distribution of the spore coat ridge. Such a result represents a first but crucial step toward correlative surface-chemistry characterization of spores via nanoscale spectroscopy. Our analysis is of potential interest for bacterial surface-display systems and for drug delivery applications.

METHODS

Data Processing. *Basis Analysis.* The application of basis analysis[49] (BA) relies on the deconvolution of each acquired spectrum $S(\nu)$ into somehow selected spectra, termed basis spectra $S_i(\nu)$, according to

$$S(\nu) = \sum_i a_i S_i(\nu) \quad (3)$$

Therefore, images are constructed by plotting the weight coefficients (or components) $a_i(x, y)$ as a function of the spatial coordinates (x, y) in the acquired hyperspectral data map. As such, these maps clarify to what extent each basis function well represents the observed initial spectrum as a function of the scan parameters (x, y). Within this study, BA was performed by using the WITec Project software,[68] based on least-squares minimization algorithm with positive constrained coefficients.

Principal Component Analysis. Principal component analysis (PCA) is a statistical tool for the analysis of multidimensional data sets.[50] It is mathematically defined as an orthogonal linear transformation mapping the initial data set into a new coordinate system such that the greatest variance of the projected data comes to lie on the first coordinate called first principal component (PC1), the second greatest variance on the second coordinate (PC2), and so on. Therefore, PCs are obtained via a matrix transformation that maximizes data variance. PCA is used to condense the information contained in a set of possibly correlated variables (*e.g.*, the observables associated with a physical state) into a set of statistically more independent, uncorrelated variables in the space of principal components. The procedure of data transformation involves the diagonalization of the covariance matrix of the initial data set; as a result, the PCs are uncorrelated data and carry the most relevant information among the initial data. The order of the PCs denotes their importance in highlighting differences within the data set. The linear combination coefficients of PCs in terms of the original variables are named loadings and express the weight of each original observable with respect to the global variance of data. The coordinates of the original data sets in the PCs space are instead referred as scores. When applied to Raman spectra, scores are used for identifying and differentiating spectral data, as, for instance, produced by repeated acquisitions or spatial scans. Differences between spectra indicate PC loading peaks in specific spectral positions that can be used to spot the correlated spectral features produced in a spatial scan. It worth noticing that spectral features which do not exhibit significant point-to-point variance (being, *e.g.*, associated with a uniform distribution of chemicals in the sample) do not appear in the PC loadings. Usually, the first three PCs are able to condensate more than 70% of the initial data information. In this work, PCA was performed by using subroutines available in the software Matlab (The MathWorks, Inc.). TERS spectra were pretreated by using a custom-made routine developed in order to eliminate spurious cosmic rays contributions and to subtract a fourth-order polynomial background contribution.

Conflict of Interest: The authors declare no competing financial interest.

Acknowledgment. We express our gratitude to Pr. Y. Huttel and Dr. L. Martinez for fruitful discussions and for supplying TERS probes. G.Z. acknowledges a postdoctoral fellowship under Grant No. "FIRB 2012-RBFR12WAPY" supported by the Italian Ministry for Education, University and Research (MIUR). This research was supported in part by "Programma STAR" of University of Naples Federico II, "Compagnia di San Paolo", and "Istituto Banco di Napoli - Fondazione."

Supporting Information Available: Additional information about spore architecture; detailed TERS spectra of the map shown in Figure 3; TERS data and analysis on other spore coat regions; additional methods. This material is available free of charge *via* the Internet at http://pubs.acs.org/.

REFERENCES AND NOTES

1. Nicholson, W. L.; Munakata, N.; Horneck, G.; Melosh, H. J.; Setlow, P. Resistance of *Bacillus* Endospores to Extreme Terrestrial and Extraterrestrial Environments. *Microbiol. Mol. Biol. Rev.* **2000**, *64*, 548–572.
2. Setlow, P. I. Will Survive: DNA Protection in Bacterial Spores. *Trends Microbiol.* **2007**, *15*, 172–180.
3. McKenney, P. T.; Driks, A.; Eichenberger, P. The *Bacillus subtilis* Spore: Assembly and Functions of the Multilayered Coat. *Nat. Rev. Microbiol.* **2013**, *11*, 33–44.
4. Watabe, K.; Imamura, D.; Kuwana, R.; Takamatsu, H.; Watabe, K. Proteins Involved in Formation of the Outermost Layer of *Bacillus subtilis* Spores. *J. Bacteriol.* **2011**, *193*, 4075–4080.
5. Warth, A. D.; Ohye, D. F.; Murrell, W. G. The Composition and Structure of Bacterial Spores. *J. Cell Biol.* **1963**, *16*, 579–592.
6. Driks, A. *Bacillus subtilis* Spore Coat. *Microbiol. Mol. Biol. Rev.* **1999**, *63*, 1–20.
7. Chen, X.; Mahadevan, L.; Driks, A.; Sahin, O. Bacillus Spores as Building Blocks for Stimuli Responsive Materials and Nanogenerators. *Nat. Nanotechnol.* **2014**, *9*, 137–141.
8. Hong, H. A.; Duc, L. H.; Cutting, S. M. The Use of Bacterial Spore Formers as Probiotics. *FEMS Microbiol. Rev.* **2005**, *29*, 813–835.
9. Stahl, S.; Uhlen, M. Bacterial Surface Display: Trends and Progresses. *Trends Biotechnol.* **1997**, *15*, 185–192.
10. Sirec, T.; Strazzulli, A.; Isticato, R.; De Felice, M.; Moracci, M.; Ricca, E. Adsorption of -galactosidase of *Alicyclobacillus acidocaldarius* on Wild Type and Mutants Spores of *Bacillus subtilis*. *Microb. Cell. Fact.* **2012**, *11*, 100–110.
11. Sirec, R.; Scotto Di Mase, D.; Mauriello, E. M. F.; De Felice, M.; Ricca, E. Amino Terminal Fusion of Heterologous Proteins to CotC Increases Display Efficiencies in the *Bacillus subtilis* Spore System. *BioTechniques* **2007**, *42*, 151–156.
12. Isticato, R.; Sirec, T.; Treppiccione, L.; Maurano, F.; De Felice, M.; Rossi, M.; Ricca, E. Non-recombinant Display of the B Subunit of the Heat Labile Toxin of *Escherichia coli* on Wild Type and Mutant Spores of *Bacillus subtilis*. *Microb. Cell. Fact.* **2013**, *12*, 98–108.
13. Kailas, L.; Terry, C.; Abbott, N.; Taylor, R.; Mullin, N.; Tzokov, S. B.; Todd, S. J.; Wallace, B. A.; Hobbs, J. K.; Moir, A.; *et al.* Surface Architecture of Spores of the Bacillus Cereus/Anthracis/Thuringiensis Family at the Subnanometer Scale. *Proc. Natl. Acad. Sci. U.S.A.* **2011**, *108*, 16014–16019.
14. Buhr, T. L.; Young, A. A.; Minter, Z. A.; Wells, C. M.; Shegogue, D. A. Decontamination of a Hard Surface Contaminated with *Bacillus anthracis* Sterne and *B. anthracis* Ames Spores Using Electrochemically Generated Liquid-Phase Chlorine Dioxide ($eClO_2$). *J. Appl. Microbiol.* **2011**, *111*, 1057–1064.
15. Plomp, M.; Leighton, T.; Wheeler, K. E.; Malkin, A. J. The High-Resolution Architecture and Structural Dynamics of *Bacillus* Spores. *Biophys. J.* **2004**, *88*, 603–608.
16. Yeo, B. S.; Stadler, J.; Schmid, T.; Zenobi, R.; Zhang, W. H. Tip-Enhanced Raman Spectroscopy - Its Status, Challenges and Future Directions. *Chem. Phys. Lett.* **2009**, *472*, 1–13.
17. Yeo, B. S.; Maedler, S.; Schmid, T.; Zhang, W. H.; Zenobi, R. Tip-Enhanced Raman Spectroscopy Can See More: The Case of Cytochrome c. *J. Phys. Chem. C* **2008**, *112*, 4867–4873.
18. Sonntag, M. D.; Klingsporn, J. M.; Garibay, L. K.; Roberts, J. M.; Dieringer, J. A.; Seideman, T.; Scheidt, K. A.; Jensen, L.; Schatz, G. C.; Van Duyne, R. P. Single-Molecule Tip-Enhanced Raman Spectroscopy. *J. Phys. Chem. C* **2012**, *116*, 478–483.
19. Stadler, J.; Schmid, T.; Zenobi, R. Nanoscale Chemical Imaging Using Top-Illumination Tip-Enhanced Raman Spectroscopy. *Nano Lett.* **2010**, *10*, 4514–4520.
20. Pozzi, E. A.; Sonntag, M. D.; Jiang, N.; Klingsporn, J. M.; Hersam, M. C.; Van Duyne, R. P. Tip-Enhanced Raman Imaging: An Emergent Tool for Probing Biology at the Nanoscale. *ACS Nano* **2013**, *7*, 885–888.
21. Treffer, R.; Bohme, R.; Deckert-Gaudig, T.; Lau, K.; Tiede, S.; Lin, X.; Deckert, V. Advances in TERS (Tip-Enhanced Raman Scattering) for Biochemical Applications. *Biochem. Soc. Trans.* **2012**, *40*, 609–614.
22. Sonntag, M. D.; Pozzi, E. A.; Jiang, N.; Hersam, M. C.; Van Duyne, R. V. Recent Advances in Tip-Enhanced Raman Spectroscopy. *J. Phys. Chem. Lett.* **2014**, *5*, 3125–3130.
23. Schmid, T.; Opilik, L.; Blum, C.; Zenobi, R. Nanoscale Chemical Imaging Using Tip-Enhanced Raman Spectroscopy: A Critical Review. *Angew. Chem., Int. Ed.* **2013**, *52*, 5940–5954.
24. Pahlow, S.; März, A.; Seise, B.; Hartmann, K.; Freitag, I.; Kämmer, E.; Böhme, R.; Deckert, V.; Weber, K.; Cialla, D.; *et al.* Bioanalytical Application of Surface- and Tip-Enhanced Raman Spectroscopy. *Eng. Life Sci.* **2012**, *12*, 131–143.
25. Deckert-Gaudig, T.; Deckert, V. Nanoscale Structural Analysis Using Tip-Enhanced Raman Spectroscopy. *Curr. Opin. Chem. Biol.* **2011**, *15*, 719–724.
26. Bailo, E.; Deckert, V. Tip-Enhanced Raman Scattering. *Chem. Soc. Rev.* **2008**, *37*, 921–930.
27. Lipiec, E.; Sekine, R.; Bielecki, J.; Kwiatek, W. M.; Wood, R. B. Molecular Characterization of DNA Double Strand Breaks with Tip-Enhanced Raman Scattering. *Angew. Chem., Int. Ed.* **2014**, *53*, 169–172.
28. Ichimura, T.; Watanabe, H.; Morita, Y.; Verma, P.; Kawata, S.; Inouye, Y. Temporal Fluctuation of Tip-Enhanced Raman Spectra of Adenine Molecules. *J. Phys. Chem. C* **2007**, *111*, 9460–9464.
29. Treffer, R.; Lin, X.; Bailo, E.; Deckert-Gaudig, T.; Deckert, V. Distinction of Nucleobases - a Tip-Enhanced Raman Approach. *Beilstein J. Nanotechnol.* **2011**, *2*, 628–637.
30. Hennemann, L. E.; Meixner, A. J.; Zhang, D. Surface- and Tip Enhanced Raman Spectroscopy of DNA. *Spectroscopy* **2010**, *24*, 119–124.
31. Domke, K. F.; Zhang, D.; Pettinger, B. Tip-Enhanced Raman Scattering of Picomole Quantities of DNA Nucleobases at Au(1 1 1). *J. Am. Chem. Soc.* **2007**, *129*, 6708–6709.
32. Rasmussen, A.; Deckert, V. Surface- and Tip-enhanced Raman Scattering of DNA Components. *J. Raman Spectrosc.* **2006**, *37*, 311–317.
33. Najjar, S.; Talaga, D.; Schue, L.; Coffinier, Y.; Szunerits, S.; Boukherroub, R.; Servant, L.; Rodriguez, L.; Bonhommeau, S. Tip-Enhanced Raman Spectroscopy of Combed Double-Stranded DNA Bundles. *J. Phys. Chem. C* **2014**, *118*, 1174–1181.
34. Zhang, D.; Domke, K.; Pettinger, B. Tip-Enhanced Raman Spectroscopic Studies of the Hydrogen Bonding Between Adenine and Thymine Adsorbed on Au(1 1 1). *ChemPhysChem* **2010**, *11*, 1662–1665.
35. Kurouski, D.; Postiglione, T.; Deckert-Gaudig, T.; Deckert, V.; Lednev, I. K. Amide I. Vibrational Mode Suppression in Surface (SERS) and Tip (TERS) Enhanced Raman Spectra of Protein Specimens. *Analyst* **138**, *6*, 1665−1673.
36. Deckert-Gaudig, T.; Deckert, V. Tip-Enhanced Raman Scattering of Histidine on Novel Silver Substrates. *J. Raman. Spectrosc.* **2009**, *40*, 1446–1451.
37. Deckert-Gaudig, T.; Rauls, E.; Deckert, V. Aromatic Amino Acid Monolayers Sandwiched Between Gold and Silver: a Combined Tip-Enhanced Raman and Theoretical Approach. *J. Phys. Chem. C* **2010**, *114*, 7412–7420.
38. Deckert-Gaudig, T.; Kömmer, E.; Deckert, V. Tracking of Nanoscale Structural Variations on a Single Amyloid Fibril with Tip-Enhanced Raman Scattering. *J. Biophot.* **2012**, *5*, 215–219.
39. Schmid, T.; Messmer, A.; Yeo, B. S.; Zhang, W. H.; Zenobi, R. Towards Chemical Analysis of Nanostructures in Biofilms II: Tip-Enhanced Raman Spectroscopy of Alginates. *Anal. Bioanal. Chem.* **2008**, *391*, 1907–1916.
40. Kurouski, D.; Deckert-Gaudig, T.; Deckert, V.; Lednev, I. K. Surface Characterization of Insulin Protofilaments and

Fibril Polymorphs Using Tip-Enhanced Raman Spectroscopy (TERS). *Biophys. J.* **2014**, *106*, 263–271.
41. Cialla, D.; Deckert-Gaudig, T.; Budich, C.; Laue, M.; Möller, R.; Naumann, D.; Deckert, V.; Popp, J. Raman to the Limit: Tip-Enhanced Raman Spectroscopic Investigation of Sinlge Tobacco Mosaic Virus. *J. Raman. Spectrosc.* **2009**, *40*, 240–243.
42. Wood, B. R.; Bailo, E.; Khiavi, M. A.; Tilley, L.; Deed, S.; Deckert-Gaudig, T.; McNaughton, D.; Deckert, V. Tip-Enhanced Raman Scattering (TERS) from Hemozoin Crystals within a Sectioned Erythrocyte. *Nano Lett.* **2011**, *11*, 1868–1873.
43. Nakata, A.; Nomoto, T.; Toyota, T.; Fujinami, M. Tip-Enhanced Raman Spectroscopy of Lipid Bilayers in Water With an Alumina- and Silver-Coated Tungsten Tip. *Anal. Sci.* **2013**, *29*, 865–869.
44. Böhme, R.; Richter, M.; Cialla, D.; Rosch, P.; Deckert, V.; Popp, J. Towards a Specific Characterisation of Components on a Cell Surface-Combined TERS: Investigations of Lipids and Human Cells. *J. Raman Spectrosc.* **2009**, *40*, 1452–1457.
45. Deckert-Gaudig, T.; Böhme, R.; Freier, E.; Sebesta, A.; Merkendorf, T.; Popp, J.; Gerwert, K.; Deckert, V. Nanoscale Distinction of Membrane Patches - a TERS Study of Halobacterium Salinarum. *J. Biophotonics* **2012**, *5*, 582–591.
46. Neugebauer, U.; Rösch, P.; Schmitt, M.; Popp, J.; Julien, C.; Rasmussen, A.; Budich, C.; Deckert, V. On the Way to Nanometer-Sized Information of the Bacterial Surface by Tip-Enhanced Raman Spectroscopy. *ChemPhysChem* **2006**, *17*, 1428–30.
47. Budich, C.; Neugebauer, U.; Popp, J.; Deckert, V. Cell Wall Investigations Utilizing Tip-Enhanced Raman Scattering. *J. Microsc.* **2008**, *229*, 533–539.
48. Richter, M.; Hedegaard, M.; Deckert-Gaudig, T.; Lampen, P.; Deckert, V. Laterally Resolved and Direct Spectroscopic Evidence of Nanometer-Sized Lipid and Protein Domains on a Single Cell. *Small* **2011**, *7*, 209–214.
49. Ong, Y. H.; Lim, M.; Liu, Q. Comparison of Principal Component Analysis and Biochemical Component Analysis in Raman Spectroscopy for the Discrimination of Apoptosis and Necrosis in K562 Leukemia Cells. *Opt. Exp.* **2012**, *20*, 22158–22171.
50. Jolliffe, I. T. *Principal Component Analysis*; Springer Verlag: Berlin, 2002.
51. Rusciano, G. Experimental Analysis of Hb Oxy-Deoxy Transition in Single Optically Stretched Red Blood Cells. *Phys. Medica* **2010**, *26*, 233–239.
52. Sahin, O.; Yong, E. H.; Driks, A.; Mahadevan, L. Physical Basis for the Adaptive Flexibility of Bacillus Spore Coats. *J. R. Soc. Interface* **2012**, *9*, 3156–3160.
53. Martinez, L.; Tello, M.; Diaz, M.; Roman, E.; Garcia, R.; Huttel, Y. Aspect-Ratio and Lateral-Resolution Enhancement in Force Microscopy by Attaching Nanoclusters Generated by an Ion Cluster Source at the End of a Silicon Tip. *Rev. Sci. Instrum.* **2011**, *82*, 023710/1–023710/7.
54. Manzano, C. V.; Caballero-Calero, O.; Hormeno, S.; Penedo, M.; Luna, M.; Martin-Gonzalez, M. S. ZnO Morphology Control by Pulsed Electrodeposition. *J. Phys. Chem. C* **2012**, *117*, 1502–1508.
55. Hormeno, S.; Penedo, M.; Vicente, C.; Luna, M. Gold Nanoparticle Coated Silicon Tips for Kelvin Probe Force Microscopy in Air. *Nanotechnology* **2013**, *24*, 395701–395701.
56. Isticato, R.; Sirec, T.; Giglio, R.; Baccigalupi, L.; Rusciano, G.; Pesce, G.; Zito, G.; Sasso, A.; De Felice, M.; Ricca, E. Flexibility of the Prograamme of Spore Coat Formation in Bacillus subtilis: Bypass of CotE Requirement by Over-Production of CotH. *PLoS One* **2013**, *8*, e74949–e74957.
57. Moretti, M.; Zaccaria, R. P.; Descrovi, E.; Das, G.; Leoncini, M.; Liberale, C.; De Angelis, F.; Di Fabrizio, E. Reflection-mode TERS on Insulin Amyloid Fibrils with Top-Visual AFM Probes. *Plasmonics* **2013**, *33*, 8–25.
58. Novotny, L.; Hecht, B. *Principles of Nano-Optics*; Cambridge University Press: Cambridge, 2006.
59. Blum, C.; Opilik, L.; Metanis, N.; Weidmann, S.; Zenobi, R. Missing Amide I Mode in Tip-Enhanced Raman Spectra of Proteins?. *J. Phys. Chem. C* **2012**, *116*, 23061–23066.
60. Blum, C.; Schmid, T.; Opilik, L.; Weidmann, S.; Fagerer, S. R.; Zenobi, R. Understanding Tip-Enhanced Raman Spectra of Biological Molecules: a Combined Raman, SERS and TERS Study. *J. Raman Spectrosc.* **2012**, *43*, 1895–1904.
61. Blum, C.; Opilik, L.; Atkin, J. M.; Braun, K.; Kämmer, S. B.; Kravtsov, V.; Kumar, N.; Lemeshko, S.; Li, J.; Luszcz, K.; *et al.* Tip-Enhanced Raman Spectroscopy - an Interlaboratory Reproducibility and Comparison Study. *J. Raman Spectrosc.* **2014**, *45*, 22–31.
62. Waller, L. N.; Fox, N.; Fox, K. F.; Fox, A.; Price, R. L. Ruthenium Red Staining for Ultrastructural Visualization of a Glycoprotein Layer Surrounding the Spore of *Bacillus anthracis* and *Bacillus subtilis*. *J. Microbiol. Methods* **2004**, *58*, 23–30.
63. Alexander, T. A.; Pellegrino, P.; Gillespie, J. B. Near-Infrared Surface-Enhanced-Raman-Scattering-Mediated Detection of Single Optically Trapped Bacterial Spores. *Appl. Spectrosc.* **2003**, *57*, 1340–1345.
64. Chada, V. G. R.; Sanstad, E. A.; Wang, R.; Driks, A. Morphogenesis of *Bacillus* Spore Surfaces. *J. Bacteriol.* **2003**, *185*, 6255–6261.
65. Plomp, M.; McCaffery, J. M.; Cheong, I.; Huang, X.; Bettegowda, C.; Kinzler, K. W.; Zhou, S.; Vogelstein, B.; Malkin, A. J. Spore Coat Architecture of Clostridium Novyi NT Spores. *J. Bacteriol.* **2007**, *189*, 6457–6468.
66. Zolock, R. A.; Li, G.; Bleckmann, C.; Burggraf, L.; Fullerc, D. C. Atomic Force Microscopy of *Bacillus* Spore Surface Morphology. *Micron* **2006**, *9*, 363–369.
67. Rogers, J. L.; Nicewander, W. A. Thirteen Ways to Look at the Correlation Coefficient. *Am. Statist.* **1995**, *42*, 59–66.
68. www.witec.de, WITec GmbH, Ulm, Germany.